
Article:
Kolo, I., Askes, H. and de Borst, R. (2017) Convergence analysis of Laplacian-based gradient elasticity in an isogeometric framework. Finite Elements in Analysis and Design, 135. pp. 56-67. ISSN: 0168-874X

https://doi.org/10.1016/j.finel.2017.07.006

Convergence analysis of Laplacian-based gradient elasticity in an isogeometric framework

Isa Kolo, Harm Askes, René de Borst

University of Sheffield, Department of Civil and Structural Engineering, Mappin Street, Sheffield S1 3JD, United Kingdom

Abstract

A convergence study is presented for a form of gradient elasticity where the enrichment is through the Laplacian of the strain, so that a fourth-order partial differential equation results. Isogeometric finite element analysis is used to accommodate the higher continuity required by the inclusion of strain gradients. A convergence analysis is carried out for the original system of a fourth-order partial differential equation. Both global refinement, using NURBS, and local refinement, using T-splines, have been applied. Theoretical convergence rates are recovered, except for a polynomial order of two, when the convergence rate is suboptimal, a result which also has been found for the (fourth-order) Cahn-Hilliard equation. The convergence analyses have been repeated for the case that an operator split is applied so that a set of two (one-way) coupled partial differential equations results. Differences occur with the results obtained for the original fourth-order equation, which is caused by the boundary conditions, which is the first time this effect has been substantiated.

Keywords: Gradient elasticity, Isogeometric analysis, NURBS, T-Splines, Convergence analysis

1. Introduction

Classical continuum mechanics assumes that the solid or the structure under consideration is of a dimension that is significantly larger than its underlying microstructure, so that microstructural effects can be ignored. When the effects of microstructure become dominant – as is the case with localised shear bands in softening geomaterials [1] – classical continuum me-

chanics is no longer sufficient. Experiments have shown that specimens of a material with the same geometry, but different dimensions, exhibit different mechanical behaviour. This is called the size effect and has been recorded for quasi-brittle materials (concrete, rock, ceramics) [2], metals [3], composites [4] and micron-scale structures [5]. Indeed, the size effect, which has been attributed to the existence of a material microstructure, is not captured by classical continuum theories. Thus, enriching the classical continuum model with an internal length scale which is related to its material microstructure, enhances its applicability. This is the motivation behind the work of Mindlin [6] and Eringen and Suhubi [7], although earlier work along the same lines has been done by the Cosserat brothers [8]. A review and historical perspective is given in [9].

In Mindlin's theory [6], twelve independent degrees of freedom at two scales of deformation were identified: three displacement components and nine microdeformation components. Three possible assumptions that can relate the microscopic deformation gradient and the macroscopic displacement were outlined. The strain energy density can be expressed as a function of strains and second derivatives of macroscopic displacements thereby obscuring the multiscale nature of the theory [6, 10, 11]. This special case defines gradient elasticity. In statics, there are two additional parameters with the dimension of length which could be related to the underlying material microstructure [12, 13]. A simplification is achieved when these two length scales are equal – an approach credited to Aifantis [14, 15]. A proper theoretical framework was provided in [16] and [17] using the principle of minimum potential energy and principle of virtual work respectively.

The Aifantis theory modifies the classical stress-strain relation by making the stress also dependent on the Laplacian of the strain, thus resulting in a fourth-order governing partial differential equation. To solve the equation, standard C^0-continuous elements cannot be used. This is because higher order terms appear in the weak form, thus requiring the derivatives of displacements to be continuous – C^1-continuity requirement. In principle, the problem can be solved by Hermitian finite elements [18, 19], mixed methods [20], meshless methods [21], penalty methods [22, 23], Langrange multipliers [24] and subdivision surfaces [25]. However, all these methods have their drawbacks in terms of efficiency or implementational convenience. Thus, it remains worthwhile to explore new methods for the implementation of gradient elasticity.

An alternative approach is to use an operator split that creates two

second-order partial differential equations. In this staggered approach [26], the solution from the first equation (classical elasticity) serves as input for the second equation which solves for the gradient-enriched variables. Since this is a set of two second order partial differential equations, it can be solved with C^0-continuous elements. It is noted that the approach suggested in Reference [26] is, strictly speaking, only applicable to an infinite body where no enforcement of boundary conditions is required [27]. Although it removes strain singularities, Skalka et al. [28] found it incapable of predicting the desired stress field around a crack in composite foams (cusp-like closure at crack tip), again pointing out issues with boundary conditions i.e. difference in boundary conditions compared with the fourth-order partial differential equation. These differences have also been pointed out in [9, 29].

These restrictions have motivated Skalka et al. [28] to propose a similar strategy for Eringen's model [30], i.e. a decoupling or one-way coupling for the two second order partial differential equations. An iterative procedure was proposed for Eringen's model (also formulated by Askes and Gutiérrez [31] as implicit gradient elasticity) with the length scale replaced by a parameter increment which is chosen to be arbitrarily small. However, the choice of the number of iterations and the convergence criterion are tied to crack properties; for an arbitrary geometry, the choices seem unclear and may likely incur high computational cost. Eringen's theory is an approximation of an earlier nonlocal integral formulation [32, 33, 34]. However, it has been shown that for certain loading conditions, fully nonlocal stress-strain laws used in modelling Euler-Bernoulli elastic beams give solutions that coincide with the standard local solution, and hence do not capture size effects [35]. This can only be avoided either by combining local and nonlocal curvatures in the constitutive equation or using a gradient elastic model. [36, 37].

When comparing the two solution strategies, a method which fulfils the C^1-continuity requirement is needed. Isogeometric Analysis [38] is an extension of finite element analysis where the spline-based shape functions used to approximate the geometry are used for the analysis as well. Although coined and standardised in [38], other works along the same lines exist [39, 40]. The original drive behind isogeometric analysis was to integrate the design and analysis processes, which has the additional benefit of capturing the exact geometry, unlike standard finite element analysis. Moreover, it comes with the advantage of ease in achieving higher degree of continuity. This is due to the Non-Uniform Rational B-Splines (NURBS) shape functions. Isogeometric analysis has been used where higher continuity is required such as

in solving the Cahn-Hilliard equation [41, 42, 43], gradient damage models [44] and also in the context of gradient elasticity [45, 46, 47, 17]. In [43], the direct fourth order Cahn-Hilliard equation and a mixed formulation with coupled equations have been studied using isogeometric analysis. The study concluded that direct discretisations of higher order partial differential equations are more efficient than mixed formulations but approximations of sufficient order are required to obtain optimal convergence rates.

This work compares convergence rates for the Aifantis gradient elasticity theory with and without operator split. The paper is organised as follows: section 2 presents the Aifantis gradient elasticity formulation including the operator-split. Section 3 starts with a brief description of NURBS and Bézier extraction in isogeometric analysis [48] before discretisation of the gradient elasticity formulation with and without operator split. In section 4, the two discretisation approaches are compared in terms of error norms and convergence rates. T-splines are introduced in section 5 and finally, some more examples using gradient elasticity are presented.

2. Laplacian-based gradient elasticity formulations

2.1. Aifantis' gradient elasticity formulation

The gradient elasticity theory of Aifantis [14, 15] is considered herein. The theory extends the classical linear elastic constitutive relations by introducing the Laplacian of the strain as follows:

$$\sigma_{ij} = D_{ijkl}(\varepsilon_{kl} - \ell^2 \varepsilon_{kl,mm}) \tag{1}$$

where σ_{ij} is the stress tensor, ε_{kl} is the strain tensor, and ℓ is a length scale parameter. D_{ijkl} is the constitutive tensor, and for an isotropic linear elastic material, it is given by:

$$D_{ijkl} = \lambda \delta_{ij}\delta_{kl} + \mu \delta_{ik}\delta_{kl} + \mu \delta_{il}\delta_{kl} \tag{2}$$

λ and μ are Lamé constants, and δ_{ij} is the Kronecker delta. The accompanying equilibrium equations are:

$$\sigma_{ij,j} + b_i = 0 \tag{3}$$

where a comma denotes partial differentiation and b_i are the body forces. Substituting the stress-strain relation, eq.(1), and assuming small displace-

ment gradients, one obtains the following fourth-order partial differential equation:

$$D_{ijkl}(u_{k,jl} - \ell^2 u_{k,jlmm}) + b_i = 0 \tag{4}$$

where u_k are the displacement components.

2.2. Ru-Aifantis theorem: Operator-split

In the staggered approach of the Ru-Aifantis theorem, the fourth-order equation in eq.(4) is split into two second order partial differential equations [9, 49]:

$$D_{ijkl}u^c_{k,jl} + b_i = 0 \tag{5}$$

$$u_k - \ell^2 u_{k,mm} = u^c_k \tag{6}$$

where u^c_k is the displacement field that obeys the classical elasticity equation eq.(5), hence the superscript $(\bullet)^c$. Eq.(5) is first solved for u^c_k and the result is used in eq.(6) to solve for u_k. Thus, there is one-way coupling between them.

3. Isogeometric finite element discretisation

In traditional finite element analysis, Lagrange polynomials serve as the basis or shape functions. Isogeometric analysis replaces these Lagrange polynomials with splines which are also used in generating the geometry. This implies that both geometry and finite element analysis are based on spline functions and hence the name isogeometric analysis. NURBS or Non-Uniform Rational B-splines is the most widely used spline technology and this influenced its choice as a starting point in the seminal work where isogeometric analysis was proposed [38].

3.1. NURBS shape functions

A NURBS curve, $\mathbf{T}(\xi)$, is defined by a set of control points $\mathbf{P} = \{P_a\}_{a=1}^n \in \mathbb{R}^d$, a knot vector with increasing parametric coordinate values $\mathbf{\Xi} = \{\xi_1, \xi_2, \ldots, \xi_{n+p+1}\}$, and a set of rational basis functions $\mathbf{R} = \{R^n_{a,p}\}_{a=1}^n$ with p being the polynomial degree, and n the number of basis functions:

$$\mathbf{T}(\xi) = \sum_{a=1}^{n} P_a R_{a,p}(\xi) \tag{7}$$

The individual coordinates of the knot vector are called knots which are analogous to nodes in standard finite elements and the interval between knots is a knot span. Unlike nodes, knots are usually not interpolatory. If the first and last knots are repeated $p+1$ times, the knots become interpolatory, and the knot vector is said to be open. The basis functions of a NURBS curve are expressed as:

$$R_{a,p}(\xi) = \frac{w_a B_{a,p}(\xi)}{\mathbf{W}(\xi)} \tag{8}$$

where $B_{a,p}$ is the B-spline basis function, w_a is the corresponding weight and $\mathbf{W}$ is the weight function given by:

$$\mathbf{W}(\xi) = \sum_{b=1}^{n} w_b B_{b,p}(\xi) \tag{9}$$

The B-spline basis is defined for $p = 0$, as:

$$B_{a,0}(\xi) = \begin{cases} 1, & \xi_a \leq \xi \leq \xi_{a+1} \\ 0, & \text{otherwise} \end{cases} \tag{10}$$

and by the Cox-de Boor recursion formula for $p > 0$:

$$B_{a,p}(\xi) = \frac{\xi - \xi_a}{\xi_{a+p} - \xi_a} B_{a,p-1}(\xi) + \frac{\xi_{a+p+1} - \xi}{\xi_{a+p+1} - \xi_{a+1}} B_{a+1,p-1}(\xi) \tag{11}$$

A NURBS geometry in $\mathbb{R}^d$ is obtained from projective transformations of B-splines in $\mathbb{R}^{d+1}$ through the weights. A NURBS curve (univariate) can be extended to a surface (bivariate) through a tensor product of the bases [38]:

$$N_{a,b}^{p,q}(\xi, \eta) = \frac{B_{a,p}(\xi) A_{b,q}(\eta) w_{a,b}}{\sum_{c=1}^{nB} \sum_{d=1}^{nA} B_{c,p}(\xi) A_{d,q}(\eta) w_{c,d}} \tag{12}$$

where $N_{a,b}^{p,q}$ is the two-dimensional NURBS basis function; η, $A_{b,q}$, and q are the knot vector, B-spline basis and the polynomial degree in the second spatial dimension respectively. The number of basis functions in the ξ and η directions are nB and nA respectively. Thus a NURBS surface, $\mathbf{S}$, is defined by replacing $R_{a,p}$ in eq.(7) by $N_{a,b}^{p,q}$:

$$\mathbf{S}(\xi,\eta) = \sum_{a=1}^{nA}\sum_{b=1}^{nB} P_{a,b} N_{a,b}^{p,q}(\xi,\eta) \tag{13}$$

A subdomain with uniform elements and material models is termed a patch. A knot vector divides a patch into elements, and hence, insertion of knots is analogous to h-refinement in standard finite elements. A knot could be inserted multiple times – knot multiplicity (k) is the number of times a certain knot is inserted. The continuity between elements is of order C^{p-k} or C^{p-1} when there are no repeated knots.

3.2. Isogeometric analysis via Bézier extraction

Through multiple knot insertion in a procedure referred to as Bézier decomposition, a NURBS mesh can be decomposed into C^0-continuous Bézier elements (Figure 1), thereby providing an element structure that can be easily incorporated in existing finite element codes. This is achieved through a linear operator $\mathbf{C}$ such that:

$$\mathbf{N}(\xi) = \mathbf{C}\mathbf{B}(\xi) \tag{14}$$

where $\mathbf{N}$ contains the NURBS basis functions, $\mathbf{B}$ contains the Bézier basis functions, and $\mathbf{C}$ is termed the Bézier extraction operator. For each nonzero knot span, the NURBS curve is decomposed into C^0-continuous Bézier elements [48]. It follows from eq.(13) that to represent any field variable using NURBS, the control point is replaced with any variable of interest:

$$\mathbf{X}(\xi,\eta) = \sum_{a=1}^{nA}\sum_{b=1}^{nB} x_{a,b} N_{a,b}^{p,q}(\xi,\eta) \tag{15}$$

where $\mathbf{X}$ is the variable of interest (e.g. displacement) and x is the value (displacement) at the control point. With this, both the geometry and solution of desired variables (analysis) use the same basis or shape functions.

It is important to note that, notwithstanding Bézier extraction being local to the element, the C^{p-k}-continuity of NURBS is maintained within a single patch. However, when more than one patch is used to represent the geometry, special techniques need to be adopted to raise the C^0-continuity that exists between patches [45].

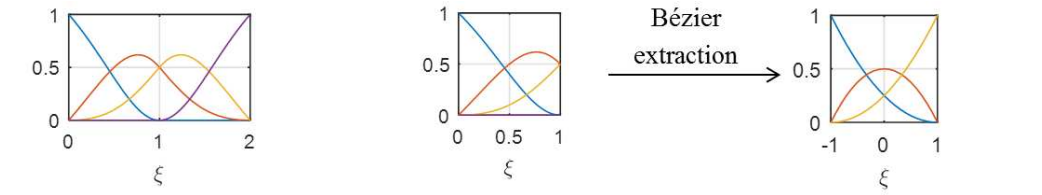

NURBS basis functions across domain (2 elements)

NURBS basis functions within element 1

Bézier element equivalent (parent domain)

Figure 1: Bézier decomposition and extraction for a quadratic NURBS curve with knot vector $\Xi = \{0, 0, 0, 1, 2, 2, 2\}$. The interior knot divides the curve into two elements. A knot of value $\{1\}$ is inserted so that the multiplicity of the interior knot equals the polynomial degree, 2. Each element is then decomposed into equivalent Bézier curves which are C^0-continuous between elements. Through the Bézier extraction operator, the Bézier finite elements ensue and are used directly in analysis.

3.3. Spatial discretisation

3.3.1. Direct discretisation

The fourth-order equation – eq.(4) – can be written in Voigt matrix notation as follows:

$$\mathbf{L}^T\mathbf{D}\mathbf{L}(\mathbf{u} - \ell^2\nabla^2\mathbf{u}) + \mathbf{b} = 0 \tag{16}$$

where $\nabla^2 \equiv \nabla^T \cdot \nabla$ is the Laplacian operator with $\nabla = [\frac{\partial}{\partial x}, \frac{\partial}{\partial y}, \frac{\partial}{\partial z}]^T$, and $\mathbf{L}$ is the differential operator:

$$\mathbf{L} = \begin{bmatrix} \frac{\partial}{\partial x} & 0 & 0 & \frac{\partial}{\partial y} & \frac{\partial}{\partial z} & 0 \\ 0 & \frac{\partial}{\partial y} & 0 & \frac{\partial}{\partial x} & 0 & \frac{\partial}{\partial z} \\ 0 & 0 & \frac{\partial}{\partial z} & 0 & \frac{\partial}{\partial x} & \frac{\partial}{\partial y} \end{bmatrix}^T \tag{17}$$

Eq.(16) is obtained directly by substituting the matrix-vector form of eq.(1),

$$\boldsymbol{\sigma} = \mathbf{D}(\boldsymbol{\varepsilon} - \ell^2\nabla^2\boldsymbol{\varepsilon}) \tag{18}$$

and the kinematic relation for small displacement gradients

$$\boldsymbol{\varepsilon} = \mathbf{L}\mathbf{u} \tag{19}$$

into the equilibrium equation in Voigt notation:

$$\mathbf{L}^T\boldsymbol{\sigma} + \mathbf{b} = \mathbf{0} \tag{20}$$

We recall that, unlike finite elements where variables are computed at the nodes, variables are computed at the control points in isogeometric analysis. Thus, the displacements $\mathbf{u} = [u_x, u_y, u_z]^T$ are related to the discrete displacements $\mathbf{a} = [a_{1x}, a_{1y}, a_{1z}, a_{2x}, a_{2y}, a_{2z}, \ldots]^T$ in the control points via:

$$\mathbf{u} = \mathbf{N}_u\mathbf{a} \tag{21}$$

where $\mathbf{N}_u$ is the matrix which contains the NURBS shape functions:

$$\mathbf{N}_u = \begin{bmatrix} N_1 & 0 & 0 & N_2 & 0 & 0 & \cdots & N_{ns} & 0 & 0 \\ 0 & N_1 & 0 & 0 & N_2 & 0 & \cdots & 0 & N_{ns} & 0 \\ 0 & 0 & N_1 & 0 & 0 & N_2 & \cdots & 0 & 0 & N_{ns} \end{bmatrix} \tag{22}$$

and ns is the number of shape functions at each control point. The number of rows corresponds to the number of degrees of freedom per control point.

To discretise eq.(16), we premultiply it by a test function $\tilde{\mathbf{u}}$ and integrate over the domain $\boldsymbol{\Omega}$:

$$\int_\Omega \tilde{\mathbf{u}}^T \Big[\mathbf{L}^T\mathbf{D}\mathbf{L}(\mathbf{u} - \ell^2\nabla^2\mathbf{u}) + \mathbf{b}\Big] d\Omega = 0 \tag{23}$$

The first term is integrated by parts and the use of Green's theorem yields [21]:

$$\begin{gathered} \int_\Omega \tilde{\boldsymbol{\varepsilon}}^T\mathbf{D}\boldsymbol{\varepsilon} d\Omega \; + \sum_{i=1}^{3} \int_\Omega \ell^2 \frac{\partial \tilde{\boldsymbol{\varepsilon}}^T}{\partial x_i}\mathbf{D}\frac{\partial \boldsymbol{\varepsilon}}{\partial x_i} d\Omega = \\ \int_\Omega \tilde{\mathbf{u}}^T\mathbf{b} d\Omega \; + \int_{\Gamma_n} \tilde{\mathbf{u}}^T\mathbf{t} d\Gamma + \sum_{i=1}^{3} \oint_\Gamma \ell^2 (\mathbf{n}\cdot\nabla\tilde{\mathbf{u}})^T\mathbf{D}\frac{\partial \boldsymbol{\varepsilon}}{\partial x_i} d\Gamma \end{gathered} \tag{24}$$

where $\mathbf{t}$ represents the prescribed tractions on the Neumann part of the boundary Γ_n and $\mathbf{n}$ is the normal vector to the boundary, cf. [24]. Next, the derivatives of $\boldsymbol{\varepsilon}$ are assumed to vanish on the boundary. Hence, the last term in eq.(24) vanishes.

In a Bubnov-Galerkin sense, the test and trial functions are discretised in the same space, so that

$$\tilde{\mathbf{u}} = \mathbf{N}_\mathrm{u}\tilde{\mathbf{a}} \tag{25}$$

Substituting eq.(25) into eq. (24), and requiring the result to hold for all admissible $\tilde{\mathbf{a}}$, the following ensues:

$$[\mathbf{K}_1 + \mathbf{K}_2]\mathbf{a} = \mathbf{f}^{ext} \tag{26}$$

where $\mathbf{K}_1$ is the standard stiffness matrix expressed as:

$$\mathbf{K}_1 = \int_\Omega \mathbf{B}^T \mathbf{D} \mathbf{B} d\Omega \tag{27}$$

and $\mathbf{B} = \mathbf{L}\mathbf{N}_u$. The higher order derivatives of the shape functions are assembled in $\mathbf{K}_2$ and are given by:

$$\mathbf{K}_2 = \sum_{i=1}^{3} \int_\Omega \ell^2 \frac{\partial \boldsymbol{B}^T}{\partial x_i} \mathbf{D} \frac{\partial \boldsymbol{B}}{\partial x_i} d\Omega \tag{28}$$

The external force vector $\mathbf{f}^{ext}$ reads:

$$\mathbf{f}^{ext} = \int_\Omega {\mathbf{N}_\mathrm{u}}^T \mathbf{b} d\Omega \; + \int_{\Gamma_n} {\mathbf{N}_\mathrm{u}}^T \mathbf{t} d\Gamma \tag{29}$$

As evident from eq.(26), C^1-continuous shape functions are required since second spatial derivatives have to be computed. This is provided automatically by the NURBS shape functions which are used in isogeometric analysis. The finite element implementation via Bézier extraction is achieved using the Jive open source C++ library [50].

3.3.2. Operator split: One-way coupling

An alternative approach is to split the fourth-order partial differential equation into a sequence of two second-order partial differential equations. In matrix-vector format, this is expressed as:

$$\mathbf{L}^T \mathbf{D} \mathbf{L} \mathbf{u}^c + \mathbf{b} = 0 \tag{30}$$

$$\mathbf{u} - \ell^2 \nabla^2 \mathbf{u} = \mathbf{u}^c \tag{31}$$

cf. eqs. (5) and (6). After resolution of eq.(30), eq.(31) can be solved for the non-local displacements $\mathbf{u}$.

To discretise eq.(30), we first premultiply it by the test function $\tilde{\mathbf{u}}^c$ and integrate by parts to obtain the weak form:

$$\int_\Omega (\mathbf{L}\tilde{\mathbf{u}}^c)^T \mathbf{D}\mathbf{L}\mathbf{u}^c d\Omega = \int_\Omega (\tilde{\mathbf{u}}^c)^T \mathbf{b} d\Omega + \int_{\Gamma_n} (\tilde{\mathbf{u}}^c)^T \mathbf{t} d\Gamma \tag{32}$$

where $\mathbf{t}$ are the prescribed tractions on the Neumann part of the boundary Γ_n. The test function and trial functions are discretised as in the previous section using NURBS shape functions:

$$\tilde{\mathbf{u}}^c = \mathbf{N}_\mathrm{u} \tilde{\mathbf{a}}^c \tag{33}$$

$$\mathbf{u}^c = \mathbf{N}_\mathrm{u} \mathbf{a}^c \tag{34}$$

where $\tilde{\mathbf{a}}^c$ and $\mathbf{a}^c$ are the displacements at the control points. For eq.(32) to hold for any $\tilde{\mathbf{a}}^c$, we derive:

$$\int_\Omega \mathbf{B}^T \mathbf{D}\mathbf{B} d\Omega \, \mathbf{a}^c = \mathbf{f}^{ext} \tag{35}$$

with $\mathbf{f}^{ext}$ the external force. $\mathbf{K}_1$ and $\mathbf{B}$ represent the standard stiffness and strain-displacement matrices, respectively, defined in the previous section.

Eq.(31) can also be expressed in terms of strains pre-multiplied by $\mathbf{DL}$. This renders a stress form of the equation [29]:

$$\boldsymbol{\sigma} - \ell^2 \nabla^2 \boldsymbol{\sigma} = \mathbf{D}\mathbf{L}\mathbf{u}^c \tag{36}$$

With the use of a test function $\tilde{\boldsymbol{\sigma}}$, one obtains the weak form:

$$\int_\Omega \left[\tilde{\boldsymbol{\sigma}}^T \boldsymbol{\sigma} + \ell^2 \sum_{i=1}^{3} \int_\Omega \frac{\partial \tilde{\boldsymbol{\sigma}}^T}{\partial x_i} \frac{\partial \boldsymbol{\sigma}}{\partial x_i} \right] d\Omega - \oint_\Gamma \tilde{\boldsymbol{\sigma}}^T \ell^2 (\mathbf{n} \cdot \nabla \boldsymbol{\sigma}) d\Gamma = \int_\Omega \tilde{\boldsymbol{\sigma}}^T \mathbf{D}\mathbf{L}\mathbf{u}^c d\Omega \tag{37}$$

where $\mathbf{n}$ is the normal vector to the boundary Γ. Assuming natural boundary conditions ($\mathbf{n} \cdot \nabla \boldsymbol{\sigma} = 0$) implies that the boundary integral term vanishes. When the usual essential boundary condition is applied, i.e. $\boldsymbol{\sigma} = \boldsymbol{\sigma}^c$, we have $\tilde{\boldsymbol{\sigma}} = \mathbf{0}$, and again, the boundary integral term vanishes.

Discretisation is achieved using the shape functions for the stresses:

$$\boldsymbol{\sigma} = \mathbf{N}_\sigma \mathbf{s} \tag{38}$$

$$\tilde{\boldsymbol{\sigma}} = \mathbf{N}_\sigma \tilde{\mathbf{s}} \tag{39}$$

where $\mathbf{s}$, $\tilde{\mathbf{s}}$ are control point variables. For three spatial dimensions, $\mathbf{N}_\sigma$ is a 6-row matrix which is an extension of the 3-row matrix $\mathbf{N}_\mathrm{u}$:

$$\mathbf{N}_\sigma = \begin{bmatrix} N_1 & 0 & 0 & 0 & 0 & 0 & N_2 & 0 & 0 & 0 & 0 & 0 & \cdots \\ 0 & N_1 & 0 & 0 & 0 & 0 & 0 & N_2 & 0 & 0 & 0 & 0 & \cdots \\ 0 & 0 & N_1 & 0 & 0 & 0 & 0 & 0 & N_2 & 0 & 0 & 0 & \cdots \\ 0 & 0 & 0 & N_1 & 0 & 0 & 0 & 0 & 0 & N_2 & 0 & 0 & \cdots \\ 0 & 0 & 0 & 0 & N_1 & 0 & 0 & 0 & 0 & 0 & N_2 & 0 & \cdots \\ 0 & 0 & 0 & 0 & 0 & N_1 & 0 & 0 & 0 & 0 & 0 & N_2 & \cdots \end{bmatrix} \tag{40}$$

Eq.(37) is therefore discretised as [49]:

$$\int_\Omega \left[{\mathbf{N}_\sigma}^T \mathbf{N}_\sigma \; + \ell^2 \sum_{i=1}^{3} \int_\Omega \frac{\partial {\mathbf{N}_\sigma}^T}{\partial x_i} \frac{\partial \mathbf{N}_\sigma}{\partial x_i} \right] d\Omega \, \mathbf{s} = \int_\Omega {\mathbf{N}_\sigma}^T \mathbf{D}\mathbf{B} d\Omega \, \mathbf{a}^c \tag{41}$$

This discretisation is also implemented via Bézier extraction using the Jive C++ library. $\mathbf{N}_\sigma$ and $\mathbf{N}_\mathrm{u}$ could in principle be chosen independently but the requirement in this case is only C^0-continuity for the shape functions. This is one attractive attribute of the Ru-Aifantis theorem which propelled its application to remove singularities in crack problems [49].

It is important to note that the second reaction-diffusion equation is associated with nonlocal or gradient-enriched strains and thus, the related gradient-enriched stresses are not necessarily in equilibrium [29, 9]. This was also pointed out by [27] where it was argued that the operator split is only valid where the body under consideration is infinite, eliminating the need to enforce any boundary conditions.

4. Errors and Convergence rates

To determine the convergence rate, the L_2 norm of the stress error is considered:

$$\|e\|_{L_2} = \left[\int_\Omega (\boldsymbol{\sigma} - \hat{\boldsymbol{\sigma}})^T (\boldsymbol{\sigma} - \hat{\boldsymbol{\sigma}}) \right]^{\frac{1}{2}} d\Omega \tag{42}$$

where $\boldsymbol{\sigma}$ is the exact solution and $\hat{\boldsymbol{\sigma}}$ is the approximated solution. For 2D classical elasticity, the theoretical convergence rate for the stress based on the total number of the degrees of freedom ($nDOF$) is $O(nDOF^{-\frac{p}{2}})$; based

on a defined mesh-parameter (h), it is $O(h^p)$ for a polynomial order of p. Prior to gradient elasticity, the convergence rates for classical elasticity are briefly presented.

A plane-strain, thick hollow cylinder subjected to external pressure is considered [19, 45]. Only a quarter of the cylinder is analysed due to symmetry (shaded region in Figure 2). The problem is illustrated in Figure 2 where $r_i = 0.05$ m is the inner radius, $r_o = 0.5$ m is the outer radius and $P = 1.0$ MPa is the applied external pressure. Young's modulus, $E = 8100$ MPa and Poisson's ratio, $\nu = 0.35$.

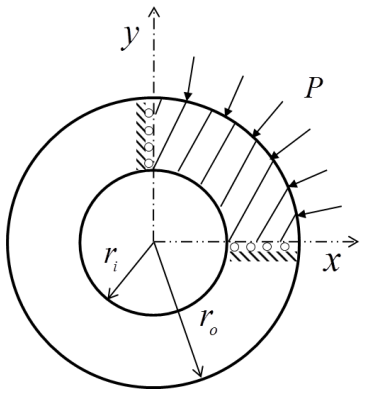

Figure 2: Geometry and boundary conditions for a thick-walled cylinder subjected to an external pressure, P

4.1. Classical elasticity

In this case where the length scale $\ell = 0$, it suffices to restrict the x-displacement [u_x(0,y)=0] at the left end and the y-displacement [$u_y(x, 0)$=0] at the bottom to achieve symmetry. Six meshes with $2^k \times 2^k$ elements, $k = 2 - 7$ have been considered. Three polynomial orders of the NURBS shape functions have been investigated: $p = 2, 3, 4$. The exact solution (plane-strain) is [51]:

$$
\begin{aligned}
u_r &= -(1+\nu)\frac{Pr_o^2}{E(r_o^2-r_i^2)}\left\{1-2\nu+\frac{r_i^2}{r^2}\right\} \\
\sigma_{rr} &= \frac{Pr_o^2}{r_o^2-r_i^2}\left(\frac{r_i^2}{r^2}-1\right) \\
\sigma_{\theta\theta} &= \frac{Pr_o^2}{r_o^2-r_i^2}\left(\frac{r_i^2}{r^2}+1\right)
\end{aligned}
\tag{43}
$$

The results are presented in Figure 3 where h_{max} is the maximum diagonal between two opposite knot locations in the physical space. It is apparent from the computed convergence rates, denoted by m, that the theoretical predictions are obtained. For example, the values of $m \approx -1.5 = -\frac{p}{2}$ and $m \approx 3 = p$ are obtained in the case of cubic NURBS ($p = 3$) considering total degrees of freedom ($nDOF$) and mesh parameter (h_{max}) respectively.

While the fourth order (direct) equation for the cylinder has an exact solution [19], for the set of second order equations, the solution can only be approximated [49]. This has been achieved using Richardson extrapolation [52], which involves using the solution of three (uniformly refined) meshes to approximate the exact solution. For a quadrilateral, it is required that each successive mesh doubles the number of elements in each direction, see Figure 4. Indeed the solution is approximated at points present in all three meshes (red boxes in Figure 4) as:

$$
f_{exact}(i,j) = \frac{1}{3}f_{\Delta x}(i,j) - 2f_{\frac{\Delta x}{2}}(i,j) + \frac{8}{3}f_{\frac{\Delta x}{4}}(i,j) \tag{44}
$$

Since Richardson extrapolation is mesh-based, variables are involved at vertex points rather than at integration points. A suitable error estimation technique is provided by the L_2-relative norm of the stress [49]:

$$
\|e\|_{L_2-relative} = \sqrt{\frac{\sum_{i=1}^{nDOF}(\sigma_i^e-\sigma_i^c)^2}{\sum_{i=1}^{nDOF}(\sigma_i^e)^2}} \tag{45}
$$

where σ^e is the exact solution, σ^c is the numerical solution and $nDOF$ is the total number of stress components. Note that for the set of second-order equations, this is the total degrees of freedom in the discretisation of the

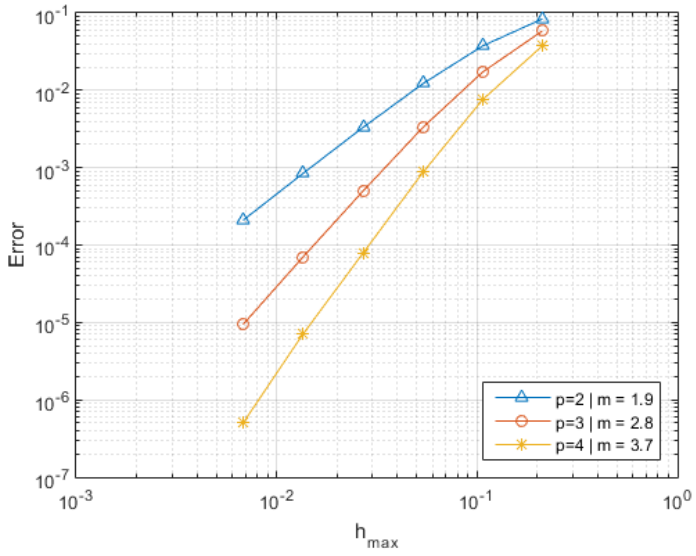

(a)

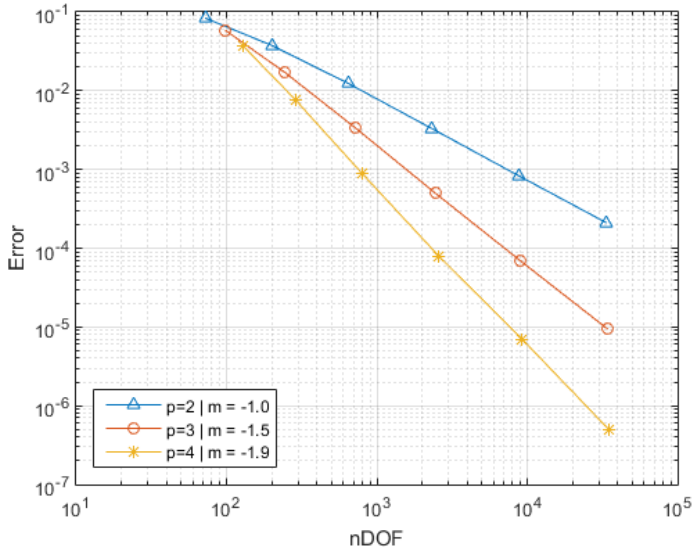

(b)

Figure 3: L^2 norm of the stress error against: (a) maximum mesh parameter; (b) total number of degrees of freedom for quadratic ($p = 2$), cubic ($p = 3$) and quartic NURBS ($p = 4$). Convergence rate is the slope (m).

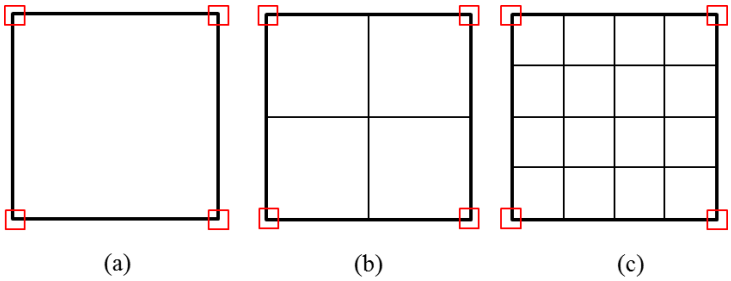

Figure 4: Richardson extrapolation. Three meshes: (a) $f_{\Delta x}$, (b) $f_{\frac{\Delta x}{2}}$, (c)$f_{\frac{\Delta x}{4}}$ are used to approximate the solution of a second order partial differential equation. The approximation points of interest (red boxes) must be present in all meshes.

second partial differential equation. The results based on Richardson extrapolation for classical elasticity are shown in Figure 5. The three finest meshes are used in approximating the solution. Again, from the slopes which represent the convergence rates, the theoretical values are retrieved fairly well. It is observed that use of the exact solution leads to slightly better results.

4.2. Gradient elasticity

The length scale parameter is taken as $\ell = 0.01$ m. Additional boundary conditions must be imposed at the left and at the bottom [19]: $\frac{\partial u_y}{\partial x} = 0$ at the left boundary and $\frac{\partial u_x}{\partial y} = 0$ at the bottom boundary. $\frac{\partial u_y}{\partial x} = 0$ is imposed by using the set of points immediately next to the boundary: $u_y(2, j) = u_y(1, j)$ [45]. Similarly, $\frac{\partial u_x}{\partial y} = 0$ is imposed by enforcing $u_x(i, 2) = u_x(i, 1)$. When the operator split is used, the first equation maintains the same boundary conditions as described for classical elasticity. In the second equation, which solves for the stresses that include the gradient effect, the additional fourth-order boundary condition is imposed as $\tau_{xy} = 0$ on the left and bottom boundaries while a Neumann boundary condition is maintained elsewhere, i.e. $\mathbf{n} \cdot \nabla \boldsymbol{\sigma} = 0$ where $\boldsymbol{\sigma} = [\sigma_{xx}, \sigma_{yy}, \tau_{xy}]^T$.

The exact solution for the fourth-order partial differential equation is given in [19] while the solution for the case with operator split (staggered approach) is approximated using Richardson extrapolation. The results based on error estimates discussed in the previous section are shown in Figure 6. The relative L^2-error norm of the stresses is used for the staggered approach while the L^2-error norm is used for the fourth-order partial differential equa-

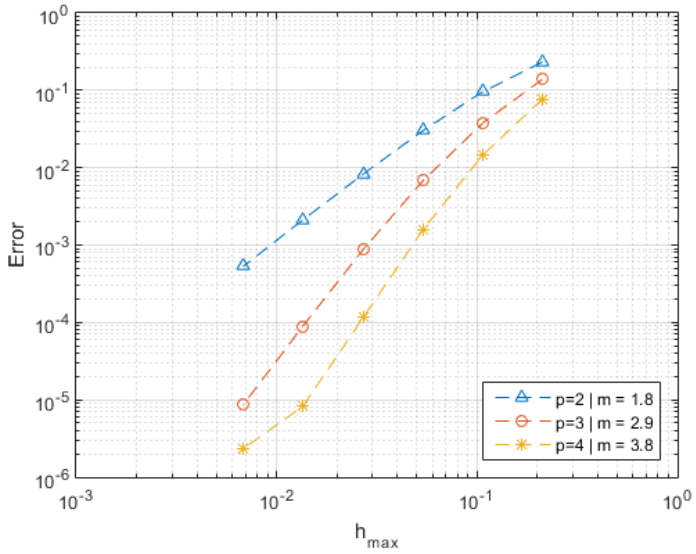

(a)

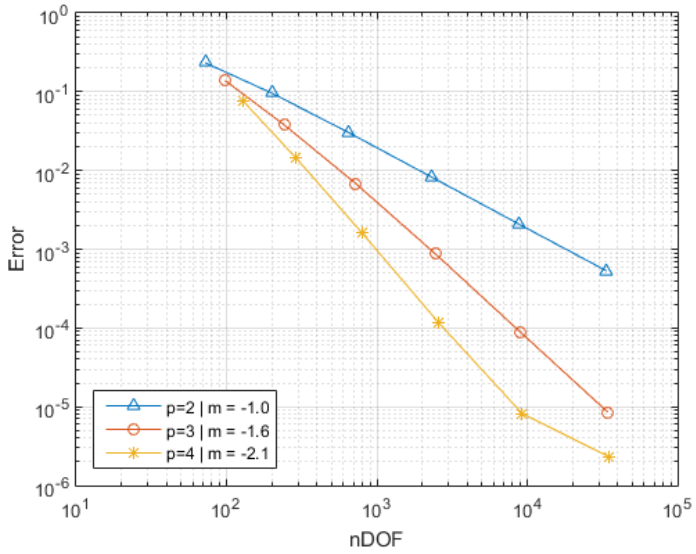

(b)

Figure 5: L^2-relative norm of the stress error against: (a) mesh parameter; (b) total number of degrees of freedom for quadratic ($p = 2$), cubic ($p = 3$) and quartic NURBS ($p = 4$). The slope (m) represents the convergence rate. Richardson extrapolation is used to approximate the exact solution.

tion (direct discretisation). The results suggest that Richardson extrapolation may not be fully appropriate for obtaining a reference solution.

On the other hand, the solutions for the direct case show the same convergence rate as with classical elasticity. It is noted that emphasis has been placed on the lower error regions in estimating the convergence rate. Another point of interest is the comparison of the convergence rates for the direct and the staggered approaches. The classical elasticity solution applies in this case to the first step of the staggered approach. Results are presented in Figure 7 using the L^2-norm of displacement error. The theoretical convergence rate for displacement is $O(h^{p+1})$ or based on the degrees of freedom, $O(nDOF^{-\frac{p+1}{2}})$, where p is the polynomial order [53]. Results in Figure 7 show a close match with theoretical prediction especially for $p = 3$ and $p = 4$. Gradient elasticity (Direct) has a suboptimal convergence rate (m) for $p = 2$ but when $p = 4$, m for the gradient case surpasses that of classical elasticity (Staggered). This indicates that, for both cases, the theoretical prediction holds. The suboptimal convergence rate observed for the direct discretisation is in accordance with the explanation given by Kästner et al. [43]. Considering a linear fourth-order partial differential equation for an infinitely continuous reference solution ($r = \infty$), the convergence rate is given by:

$$\|u - \hat{u}\|_{H^0 \equiv L^2} \leq C_0 h^{min\{p+1, 2(p-1)\}} \|u\|_{H^r} \tag{46}$$

where u is the exact displacement, $\hat{u}$ is the numerical solution and p is the polynomial order. Optimal convergence rate is thus the minimum of $\{p + 1, 2(p-1)\}$ which is $2(p-1) = 2$ for a polynomial order of two. This is in line with the result depicted in Figure 7(a).

5. Gradient elasticity with T-Splines

5.1. T-splines and T-mesh

The T-spline technology is based on the notion of a T-mesh [54, 55] which is composed of quadrilateral-shaped elements [55, 56] in two-dimensions (Figure 8). Each element in the T-mesh has one or more edges split by T-junctions. T-junctions are analogous to hanging nodes in finite elements where an internal node has less than four linked neighbours. Each T-vertex is associated with a control point and control weight. Valid knot intervals are defined which ensure that opposite sides of an element in the T-mesh have knot intervals summing to the same value (i.e. $a_1 + a_2 = b$ in Figure 8).

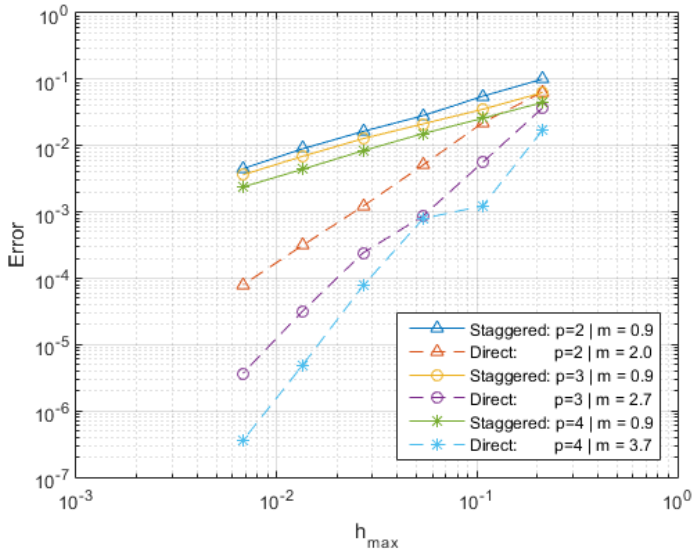

(a)

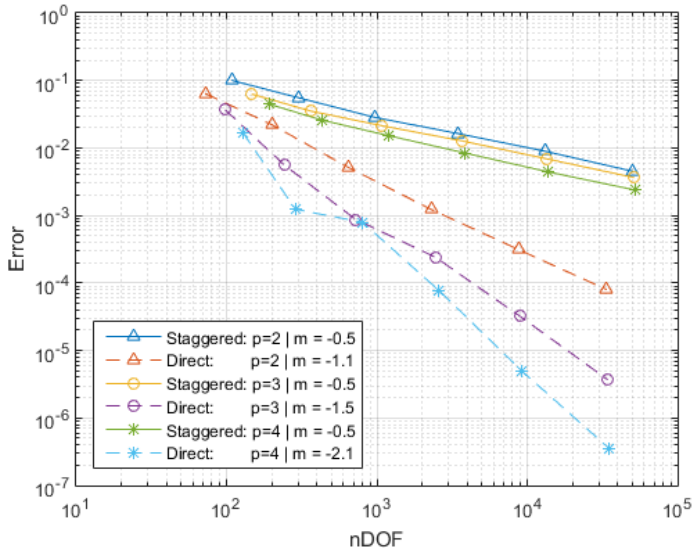

(b)

Figure 6: Error in the stress against: (a) mesh parameter; (b) total number of degrees of freedom for quadratic ($p = 2$), cubic ($p = 3$) and quartic NURBS ($p = 4$). The slope (m) represents the convergence rate. While the exact solution of the fourth order partial differential equation (Direct) is based on the exact solution, the solution for the approach with the operator split (Staggered) is based on Richardson extrapolation.

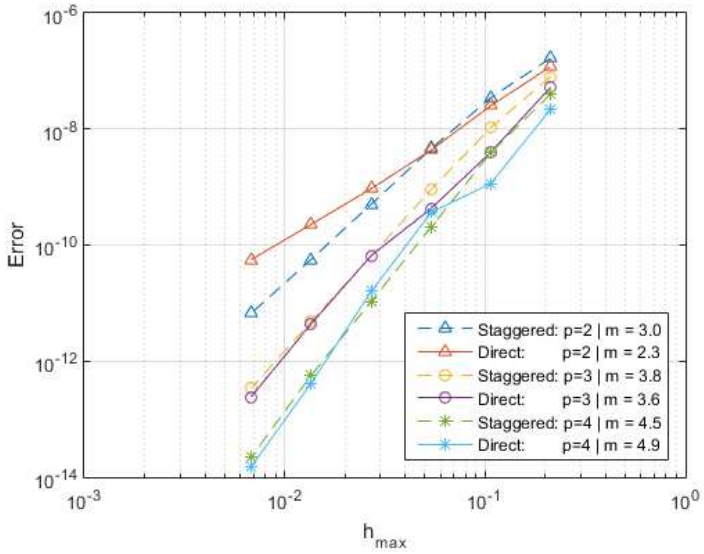

(a)

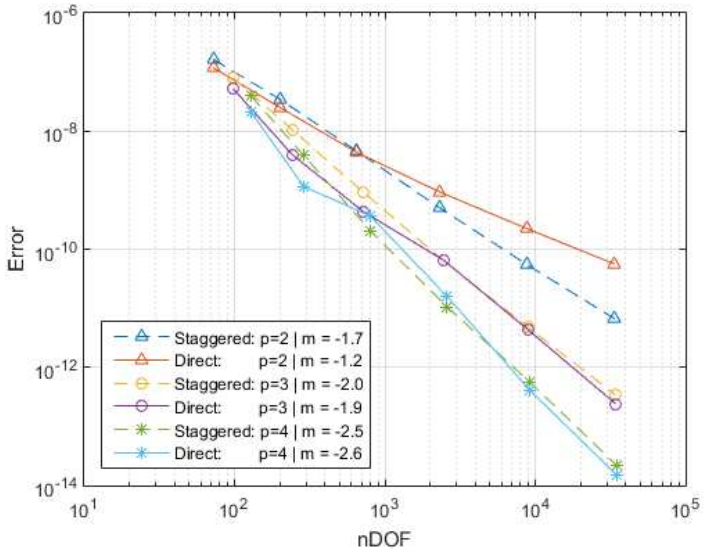

(b)

Figure 7: L^2 norm of the displacement error against: (a) maximum mesh parameter; (b) total number of degrees of freedom for quadratic ($p = 2$), cubic ($p = 3$) and quartic NURBS ($p = 4$). The slope (m) is the convergence rate.

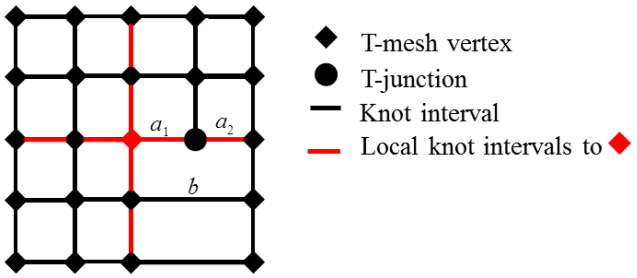

Figure 8: Illustration of T-mesh and local knot intervals, p=3

To define the T-spline basis function, local knot interval vectors are used. Unlike NURBS, T-splines are not based on a global tensor product. Each vertex has its local interval vector which is a sequence of knot intervals, $\boldsymbol{\Delta\Xi} = \{\Delta\xi_1, \Delta\xi_2, \ldots, \Delta\xi_{p+1}\}$ such that $\Delta\xi_i = \xi_{i+1} - \xi_i$ [55], where p is the polynomial degree ($p+1=4$). A set of local knot intervals for each vertex A is constructed by moving in each topological direction from the vertex until $p-1=2$ vertices or perpendicular edges are intersected. In the case where a T-mesh boundary is crossed before $p-1=2$ knot intervals are intersected, the local knot interval is set to zero. This makes the T-mesh boundary to have open knot vectors.

From the local knot interval vectors, a local knot vector is defined as $\boldsymbol{\Xi}_{\mathrm{A}} = \{\Xi_A^i\}_{i=1}^d$ and $\Xi_A^i = \{\xi_1^i, \xi_2^i, \ldots, \xi_{p+2}^i\}$ where $\xi_1^i = 0, \xi_2^i = \Delta\xi_1^i$ and for $n \geq 3$, $\xi_n^i = \Delta\xi_{n-1}^i + \Delta\xi_{n-2}^i + \ldots + \Delta\xi_1^i$. Each T-spline basis function is defined over a local basis function domain $\hat{\boldsymbol{\Omega}}_A \in \mathbb{R}^d$ by the local knot vector:

$$\hat{\boldsymbol{\Omega}}_A = \bigotimes_{i=1}^{d} \hat{\Omega}_A^i \tag{47}$$

where $\hat{\Omega}_A^i = \left[0, \Delta\xi_{p+1}^i + \ldots + \Delta\xi_2^i + \Delta\xi_1^i\right] \subset \mathbb{R}$ for polynomial degree (p). A coordinate system called the basis coordinate system is defined for each local basis function: $\boldsymbol{\xi}_{\mathrm{A}} = (\xi_A^1, \xi_A^2) = (\xi_A, \eta_A)$. With this localisation, the basis function of a T-spline is defined over each local basis function domain in the same way as NURBS, by employing Cox-de-Boor recursion formula. Also, Bézier extraction is extensible to T-splines [56].

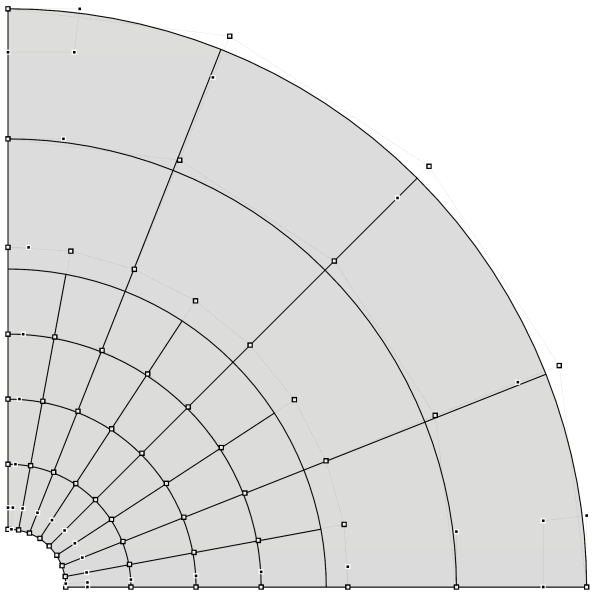

Figure 9: T-Spline representation of quarter cylinder.

5.2. Thick hollow cylinder subjected to external pressure

The problem of a thick hollow cylinder subjected to external pressure is revisited. The T-spline geometry generated using the Rhino T-Spline plug-in [57] is presented in Figure 9. Both classical and gradient elasticity are considered. For the additional boundary condition required in gradient elasticity, the immediate vertex after the boundary is used as with NURBS. Two finer meshes have been generated to qualitatively show the errors in the displacement, see Figure 10. Evidently, the convergence rate is similar to that obtained with NURBS. A representative plot of σ_{xx} is presented in Figure 11 for the direct and the staggered approach.

5.3. L-shaped panel subjected to traction

An L-shaped panel subjected to traction is considered next, Figure 12. The length and traction are $a = 30$ m and $t = 1$ MPa respectively. Essential boundary conditions are imposed as displacements on the top ($u_y = 0$) and right edge ($u_x = 0$). As in the previous problem, $E = 8100$ MPa, $\nu = 0.35$ and $\ell = 0.01$ m. The T-mesh with local refinement is depicted in Figure 12(b). This illustrates the flexibility of T-splines, and the ensuing lower computational cost.

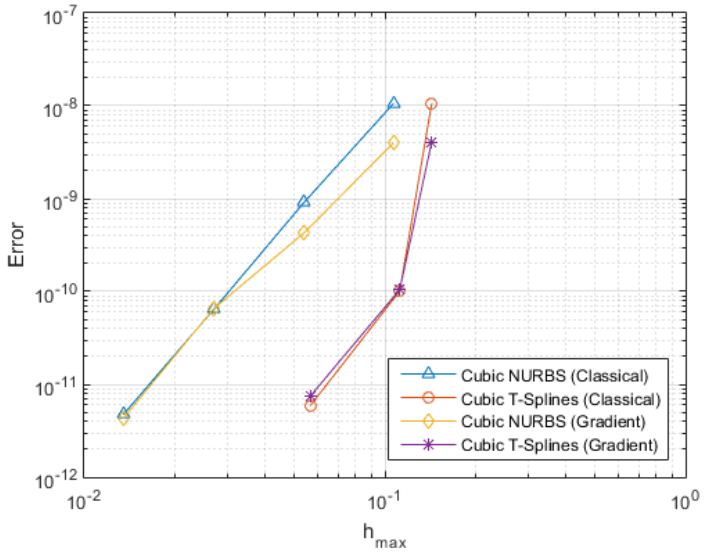

(a)

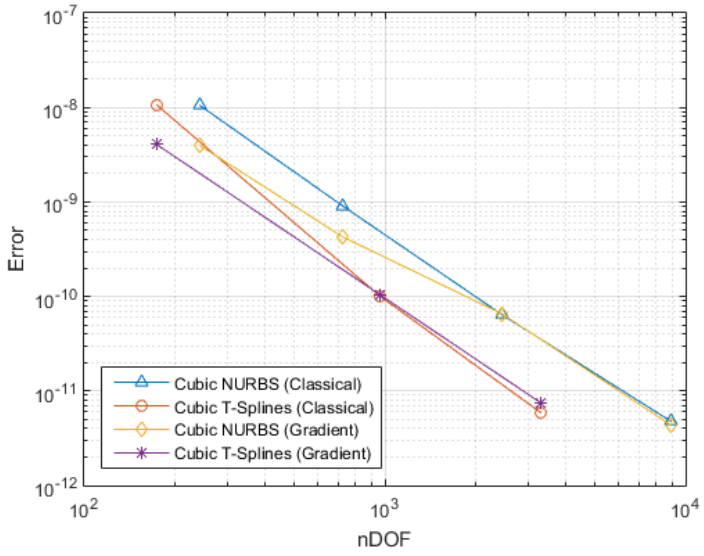

(b)

Figure 10: L^2 norm of the displacement error against: (a) maximum mesh parameter; (b) total number of degrees of freedom for cubic NURBS and T-Splines.

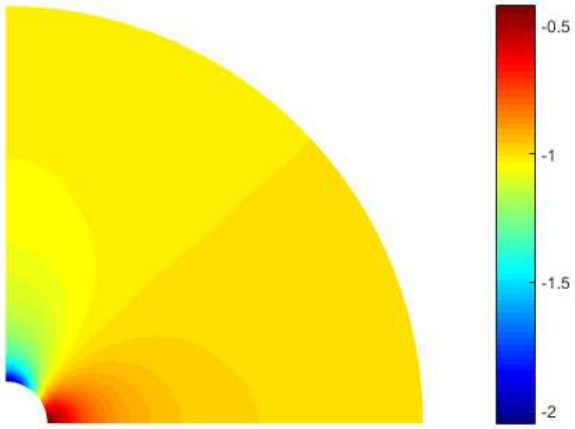

(a)

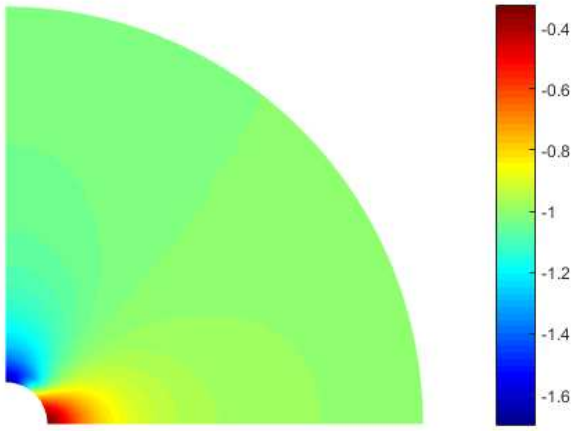

(b)

Figure 11: σ_{xx}-components of stress [MPa]: (a) direct discretisation; (b) staggered approach.

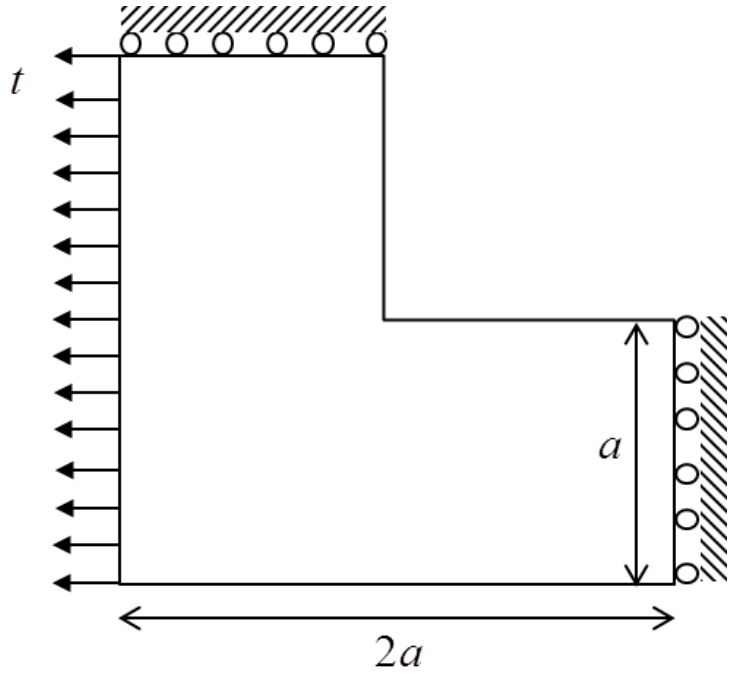

(a)

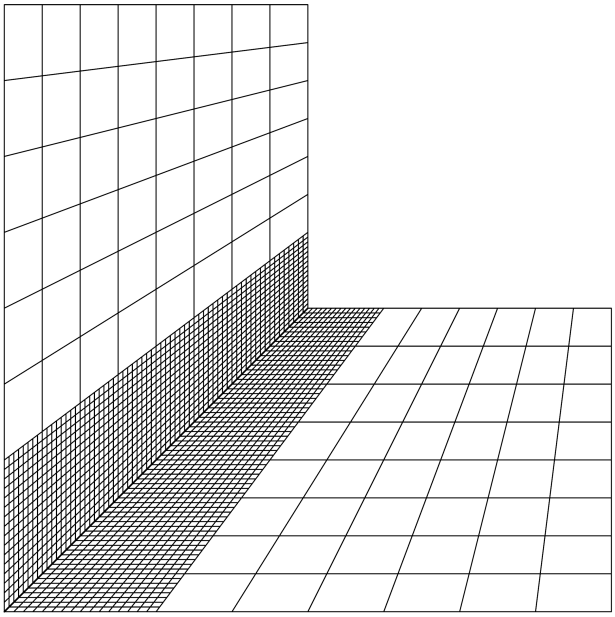

(b)

Figure 12: L-shaped panel: (a) Geometry and boundary conditions; (b) T-mesh.

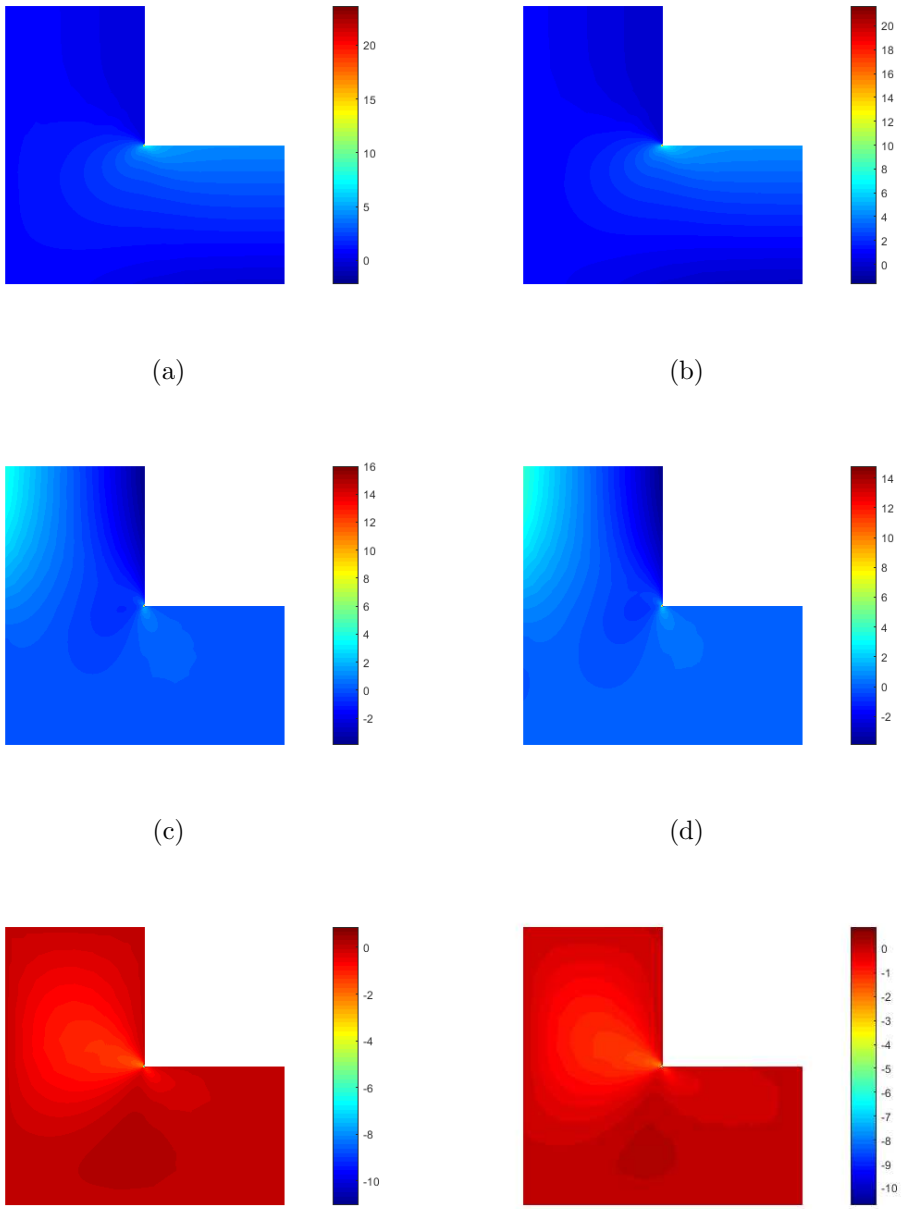

Figure 13: Stresses [MPa] in L-shaped panel using the Staggered – $(\cdot)^S$ and Direct – $(\cdot)^D$ approaches: (a) σ^D_{xx}; (b) σ^S_{xx}; (c) σ^D_{yy}; (d) σ^S_{yy}; (e) σ^D_{xy}; (f) σ^S_{xy}

The three stress components using direct discretisation and using the operator split are shown in Figure 13. There is only a slight variation in the stress distribution between the two discretisation schemes. The difference is minimal due to absence of any boundary condition required in the second step of the operator-split approach. This is in line with the argument that the latter works best when there is no need to impose boundary conditions [27], i.e. $\mathbf{n} \cdot \nabla \boldsymbol{\sigma} = 0$ everywhere.

The effect of varying the length scale parameter (ℓ) on σ_{xy} is shown in Figure 14. For lower values of ℓ, the region of high stress is obviously more localised. Results are presented for both discretisation schemes. It is noted that even when $\ell = 0$, the stress contours are not exactly identical. This could be attributed to the difference in discretised variable – while displacement is discretised in the direct approach, the stress is discretised in the staggered approach.

6. Conclusion

This study presents a convergence analysis of the Laplacian-based gradient elasticity theory. Both direct discretisation of the fourth-order partial differential equation and an operator split approach have been considered. The analyses have been carried out in an isogeometric framework for global refinement using NURBS shape functions, and for local refinement using T-splines. These shape functions naturally provide the smoothness required for the direct discretisation of the fourth-order partial differential equation. Direct discretisation shows better convergence rates for polynomial orders greater than two and follows theoretical predictions. For a polynomial order equal to two, recent results for the (fourth-order) Cahn-Hilliard equation are confirmed, i.e. that the convergence rate is suboptimal [43]. Results from the numerical examples support the argument that, strictly speaking, the operator split approach only applies to an infinite body where boundary conditions do not need to be imposed.

References

[1] H. Mühlhaus, I. Vardoulakis, The thickness of shear bands in granular materials, Geotechnique 37 (1987) 271–283.

[2] Z. P. Bazant, J. Planas, Fracture and Size Effect in Concrete and other Quasibrittle Materials, CRC Press, Boca Raton, 1997.

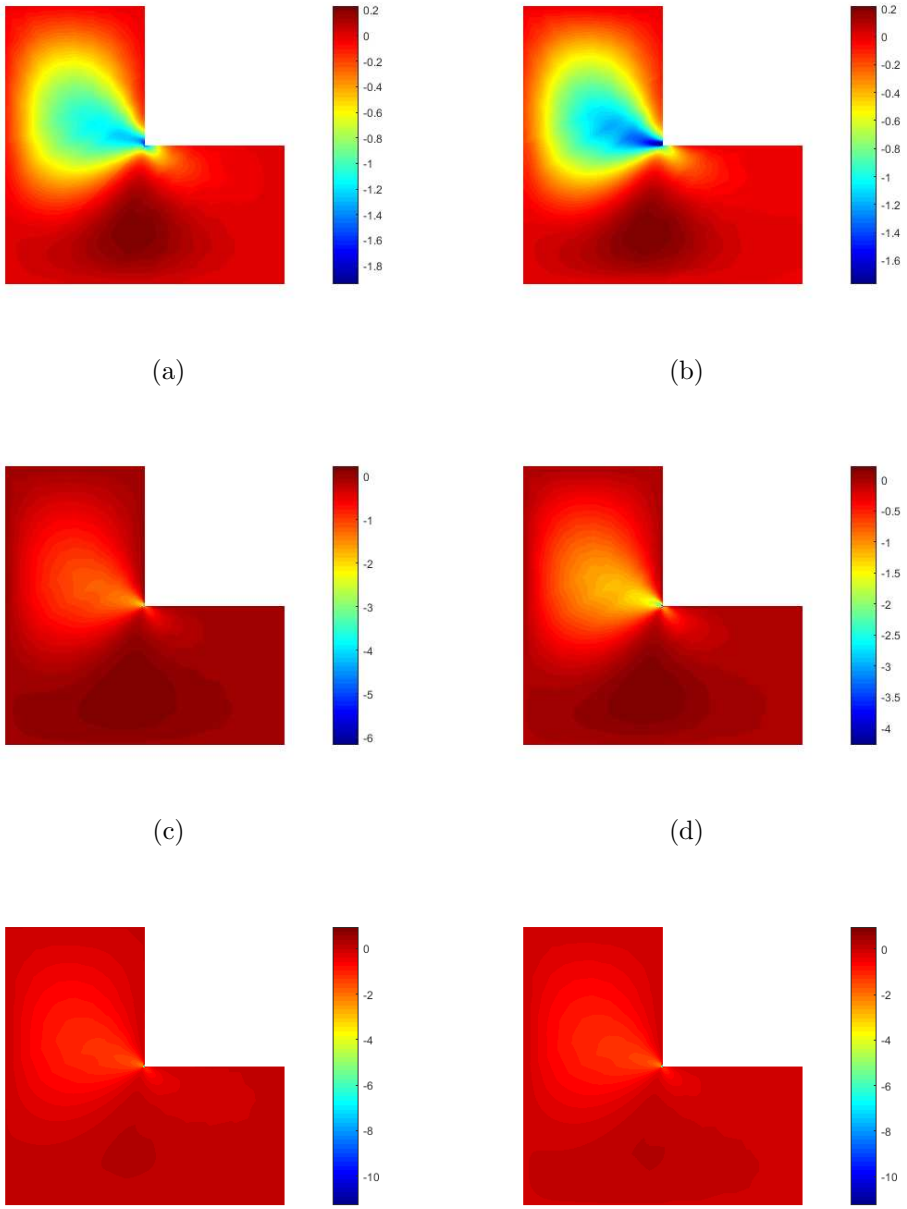

Figure 14: σ_{xy} [MPa] distribution in L-shaped panel with varying length scales (ℓ) for Staggered – $(\cdot)^S$ and Direct – $(\cdot)^D$ approach: (a) $\ell^D = 1.0$ m; (b) $\ell^S = 1.0$ m; (c) $\ell^D = 0.1$ m; (d) $\ell^S = 0.1$ m; (e) $\ell^D = 0.0$ m; (f) $\ell^S = 0.0$ m.

.

[3] A. Lasalmonie, J. Strudel, Influence of grain size on the mechanical behaviour of some high strength materials, Journal of Materials Science 21 (1986) 1837–1852.

[4] T. Okabe, N. Takeda, Size effect on tensile strength of unidirectional CFRP composites–experiment and simulation, Composites Science and Technology 62 (2002) 2053–2064.

[5] D. C. C. Lam, F. Yang, A. Chong, J. Wang, P. Tong, Experiments and theory in strain gradient elasticity, Journal of the Mechanics and Physics of Solids 51 (2003) 1477–1508.

[6] R. D. Mindlin, Micro-structure in linear elasticity, Archive for Rational Mechanics and Analysis 16 (1964) 51–78.

[7] A. C. Eringen, E. Suhubi, Nonlinear theory of simple micro-elastic solids–I, International Journal of Engineering Science 2 (1964) 189–203.

[8] E. Cosserat, F. Cosserat, Théorie des Corps Déformables, Hermann et fils, Paris, 1909.

[9] H. Askes, E. C. Aifantis, Gradient elasticity in statics and dynamics: An overview of formulations, length scale identification procedures, finite element implementations and new results, International Journal of Solids and Structures 48 (2011) 1962–1990.

[10] R. Mindlin, N. Eshel, On first strain-gradient theories in linear elasticity, International Journal of Solids and Structures 4 (1968) 109–124.

[11] R. A. Toupin, Elastic materials with couple-stresses, Archive for Rational Mechanics and Analysis 11 (1962) 385–414.

[12] P. Casal, La capillarité interne, Cahier du groupe Français de rhéologie, CNRS VI 3 (1961) 31–37.

[13] J. Sulem, I. Vardoulakis, Bifurcation Analysis in Geomechanics, CRC Press, Glasgow, 2004.

[14] E. C. Aifantis, On the role of gradients in the localization of deformation and fracture, International Journal of Engineering Science 30 (1992) 1279–1299.

[15] B. Altan, E. Aifantis, On some aspects in the special theory of gradient elasticity, Journal of the Mechanical Behavior of Materials 8 (1997) 231–282.

[16] X.-L. Gao, S. Park, Variational formulation of a simplified strain gradient elasticity theory and its application to a pressurized thick-walled cylinder problem, International Journal of Solids and Structures 44 (2007) 7486–7499.

[17] J. Niiranen, S. Khakalo, V. Balobanov, A. H. Niemi, Variational formulation and isogeometric analysis for fourth-order boundary value problems of gradient-elastic bar and plane strain/stress problems, Computer Methods in Applied Mechanics and Engineering 308 (2016) 182–211.

[18] S.-A. Papanicolopulos, A. Zervos, I. Vardoulakis, A three-dimensional C1 finite element for gradient elasticity, International Journal for Numerical Methods in Engineering 77 (2009) 1396–1415.

[19] A. Zervos, S.-A. Papanicolopulos, I. Vardoulakis, Two finite-element discretizations for gradient elasticity, Journal of Engineering Mechanics 135 (2009) 203–213.

[20] E. Amanatidou, N. Aravas, Mixed finite element formulations of strain-gradient elasticity problems, Computer Methods in Applied Mechanics and Engineering 191 (2002) 1723–1751.

[21] H. Askes, E. C. Aifantis, Numerical modeling of size effects with gradient elasticity-formulation, meshless discretization and examples, International Journal of Fracture 117 (2002) 347–358.

[22] A. Zervos, Finite elements for elasticity with microstructure and gradient elasticity, International Journal for Numerical Methods in Engineering 73 (2008) 564–595.

[23] T. Matsushima, R. Chambon, D. Caillerie, Large strain finite element analysis of a local second gradient model: Application to localization, International Journal for Numerical Methods in Engineering 54 (2002) 499–521.

[24] J. Y. Shu, W. E. King, N. A. Fleck, Finite elements for materials with strain gradient effects, International Journal for Numerical Methods in Engineering 44 (1999) 373–391.

[25] F. Cirak, M. Ortiz, P. Schroder, Subdivision surfaces: A new paradigm for thin-shell finite-element analysis, International Journal for Numerical Methods in Engineering 47 (2000) 2039–2072.

[26] C. Ru, E. Aifantis, A simple approach to solve boundary-value problems in gradient elasticity, Acta Mechanica 101 (1993) 59–68.

[27] M. Lazar, D. Polyzos, On non-singular crack fields in Helmholtz type enriched elasticity theories, International Journal of Solids and Structures 62 (2015) 1–7.

[28] P. Skalka, P. Navrátil, M. Kotoul, Novel approach to FE solution of crack problems in the Laplacian-based gradient elasticity, Mechanics of Materials 95 (2016) 28–48.

[29] H. Askes, I. Morata, E. C. Aifantis, Finite element analysis with staggered gradient elasticity, Computers & Structures 86 (2008) 1266–1279.

[30] A. C. Eringen, On differential equations of nonlocal elasticity and solutions of screw dislocation and surface waves, Journal of Applied Physics 54 (1983) 4703–4710.

[31] H. Askes, M. A. Gutiérrez, Implicit gradient elasticity, International Journal for Numerical Methods in Engineering 67 (2006) 400–416.

[32] A. C. Eringen, B. S. Kim, Stress concentration at the tip of crack, Mechanics Research Communications 1 (1974) 233–237.

[33] A. C. Eringen, C. Speziale, B. Kim, Crack-tip problem in non-local elasticity, Journal of the Mechanics and Physics of Solids 25 (1977) 339–355.

[34] R. Abdollahi, B. Boroomand, Nonlocal elasticity defined by Eringen's integral model: Introduction of a boundary layer method, International Journal of Solids and Structures 51 (2014) 1758–1780.

[35] J. Peddieson, G. R. Buchanan, R. P. McNitt, Application of nonlocal continuum models to nanotechnology, International Journal of Engineering Science 41 (2003) 305–312.

[36] N. Challamel, C. Wang, The small length scale effect for a non-local cantilever beam: A paradox solved, Nanotechnology 19 (2008) 345703.

[37] E. Benvenuti, A. Simone, One-dimensional nonlocal and gradient elasticity: Closed-form solution and size effect, Mechanics Research Communications 48 (2013) 46–51.

[38] T. J. Hughes, J. A. Cottrell, Y. Bazilevs, Isogeometric analysis: CAD, finite elements, NURBS, exact geometry and mesh refinement, Computer Methods in Applied Mechanics and Engineering 194 (2005) 4135–4195.

[39] K. Höllig, Finite Element Methods with B-Splines, SIAM, Philadelphia, 2003.

[40] X. Zhou, J. Lu, NURBS-based galerkin method and application to skeletal muscle modeling, in: Proceedings of the 2005 ACM Symposium on Solid and Physical Modeling, SPM '05, ACM, New York, NY, USA, 2005, pp. 71–78.

[41] H. Gómez, V. M. Calo, Y. Bazilevs, T. J. Hughes, Isogeometric analysis of the Cahn–Hilliard phase-field model, Computer Methods in Applied Mechanics and Engineering 197 (2008) 4333–4352.

[42] J. Liu, L. Dedè, J. A. Evans, M. J. Borden, T. J. Hughes, Isogeometric analysis of the advective Cahn–Hilliard equation: Spinodal decomposition under shear flow, Journal of Computational Physics 242 (2013) 321–350.

[43] M. Kästner, P. Metsch, R. de Borst, Isogeometric analysis of the Cahn–Hilliard equation–a convergence study, Journal of Computational Physics 305 (2016) 360–371.

[44] C. V. Verhoosel, M. A. Scott, T. J. Hughes, R. de Borst, An isogeometric analysis approach to gradient damage models, International Journal for Numerical Methods in Engineering 86 (2011) 115–134.

[45] P. Fischer, M. Klassen, J. Mergheim, P. Steinmann, R. Müller, Isogeometric analysis of 2D gradient elasticity, Computational Mechanics 47 (2011) 325–334.

[46] M. Malagù, E. Benvenuti, C. Duarte, A. Simone, One-dimensional nonlocal and gradient elasticity: Assessment of high order approximation schemes, Computer Methods in Applied Mechanics and Engineering 275 (2014) 138–158.

[47] S. Rudraraju, A. van der Ven, K. Garikipati, Three-dimensional isogeometric solutions to general boundary value problems of Toupin's gradient elasticity theory at finite strains, Computer Methods in Applied Mechanics and Engineering 278 (2014) 705–728.

[48] M. J. Borden, M. A. Scott, J. A. Evans, T. J. Hughes, Isogeometric finite element data structures based on Bézier extraction of NURBS, International Journal for Numerical Methods in Engineering 87 (2011) 15–47.

[49] C. Bagni, H. Askes, Unified finite element methodology for gradient elasticity, Computers & Structures 160 (2015) 100–110.

[50] Dynaflow Research Group, Jive v2.2, 2016. http://www.jem-jive.com/.

[51] P. L. Gould, Introduction to Linear Elasticity, Springer, New York, 3 edition, 2013.

[52] L. F. Richardson, The approximate arithmetical solution by finite differences of physical problems involving differential equations, with an application to the stresses in a masonry dam, Philosophical Transactions of the Royal Society of London. Series A 210 (1911) 307–357.

[53] J. Zhu, Z. Taylor, O. Zienkiewicz, The Finite Element Method: Its Basis and Fundamentals, Butterworth-Heinemann, Oxford, 7 edition, 2013.

[54] T. W. Sederberg, J. Zheng, A. Bakenov, A. Nasri, T-splines and T-NURCCs, ACM Transactions on Graphics 22 (2003) 477–484.

[55] M. Scott, X. Li, T. Sederberg, T. Hughes, Local refinement of analysis-suitable T-splines, Computer Methods in Applied Mechanics and Engineering 213 (2012) 206–222.

[56] M. A. Scott, M. J. Borden, C. V. Verhoosel, T. W. Sederberg, T. J. Hughes, Isogeometric finite element data structures based on Bézier extraction of T-splines, International Journal for Numerical Methods in Engineering 88 (2011) 126–156.

[57] Autodesk Inc., 2011. http://www.tsplines.com/products/tsplines-for-rhino.html.